Observation and characterization of the vestige of the jamming transition in a thermal three-dimensional system

Thomas A. Caswell,[1] Zexin Zhang,[2] Margaret L. Gardel,[1] and Sidney R. Nagel[1]

[1]*The James Franck Institute and Department of Physics, The University of Chicago, Chicago, Illinois 60637, USA*

[2]*Center for Soft Condensed Matter Physics and Interdisciplinary Research, Soochow University, Suzhou 215006, People's Republic of China*

We study the dependence on the packing fraction of the pair-correlation function $g(r)$ and particle mobility in a dense three-dimensional packing of soft colloids made of poly N-isopropyl acrylamide (pNIPAM), a thermosensitive gel. We find that $g(r)$ for our samples is qualitatively like that of a liquid at all packing fractions. There is a peak in g_1, the height of the first peak of $g(r)$, as a function of the packing fraction. This peak is identified as a vestige, which remains at finite temperature, of the divergence found at the jamming transition in simulations of soft frictionless spheres at zero temperature. As the density is increased, the particle dynamics slow down and near the packing fraction where there is a peak in g_1 the particles become arrested on the time scale of the experiment.

I. INTRODUCTION

From hard-packed granular roadbeds to glass lookout ledges in skyscrapers, amorphous materials are used as solid support structures. Yet we do not understand the origin of rigidity in those materials. In the case of crystalline solids, the onset of rigidity is a consequence of the breaking of translational symmetries during the fluid-to-crystal transition [1]. In contrast, no obvious symmetries are broken in the transition of a fluid to an amorphous solid. Indeed, an instantaneous snapshot of the structure is remarkably unaffected by the transition [2]. Is there any structural signature, however subtle, that can be identified with the onset of rigidity? Previous work has searched for such a signature in the pair-correlation function $g(r)$. Different criteria have been proposed. These include the splitting of the second peak of $g(r)$ into two subpeaks [3], the ratio of the first minimum to the first maximum of $g(r)$ [4,5], and changes to the contact-force distribution which is related to $g(r)$ at small r [6].

Recent simulations of jamming have suggested another structural signature for rigidity onset. To produce an amorphous jammed solid, a dilute system of particles is compressed until the particles are no longer free to rearrange without traversing a potential energy barrier [7]. A great deal of effort has been devoted to understanding the jamming transition at temperature $T = 0$ where there is no thermal motion [8,9]. The rigidification of random packings of finite-range soft repulsive spheres at $T = 0$ is controlled by the packing fraction ϕ. Such packings have a sharp jamming transition at a critical packing fraction ϕ_c, where the particles first unavoidably make contact [10]. Below ϕ_c all particles are sufficiently separated so that no particles overlap whereas above ϕ_c particles must overlap with their nearest neighbors. In the second case the system supports stress and can no longer rearrange without energy cost. For large system sizes and a given preparation protocol, the value of ϕ_c is well defined. However, different protocols can produce measurable variations in the average value of ϕ_c [11,12].

This onset of rigidity at $T = 0$, which is a purely geometric effect, has a distinct signature in the pair-correlation function

that is independent of the form of the repulsive force between overlapping particles. At ϕ_c all nearest-neighbor pairs are separated by precisely one particle diameter. This leads to a δ function in $g(r)$ at its first peak. This divergence is a signature of the jamming transition at $T = 0$; varying ϕ above or below ϕ_c suppresses the divergence. In this paper we focus on how a finite temperature affects this divergence.

The relevance of the $T = 0$ jamming transition to systems at finite temperature, as well as its relation to dynamical arrest and the glass transition, has not been clear. The inclusion of thermal effects has important consequences. In a thermal system the overlap of particles can be created not only by direct external compression of the system but also by thermal motion as the particles vibrate and collide with one another. Moreover, a thermal system evolves in time and can visit numerous minima in the potential-energy landscape as it traverses potential-energy barriers. What average properties of the single minima behavior remain as the system evolves over time? What vestiges of the divergence in $g(r)$, a $T = 0$ structural signature of the jamming transition, remain as the temperature is increased? Some of these issues have been addressed in a two-dimensional sample [13]. Our present work extends those results to a three-dimensional system.

Dense suspensions of hard colloids have been thoroughly studied in the context of the colloidal glass transition and supercooled fluids [3,14–25]. However, hard colloids are ill suited for studying many aspects of jamming. Since they cannot overlap they can only access configurations with $\phi < \phi_c$. (We note here, however, that the configurations at the $T = 0$ jamming transition in soft-sphere systems are allowable hard-sphere configurations as well.) In this paper, we study a three-dimensional packing of soft colloids made from a thermosensitive hydrogel. Our particles are small enough to undergo Brownian motion and thus can be considered to be at a finite temperature. We use optical confocal microscopy and particle-tracking techniques to determine the positions and displacements of particles to calculate the pair-correlation function $g(r)$ and the particle mobility.

To investigate the structure of our samples as a function of packing fraction, we control ϕ by varying the particle

diameter at a fixed number density. As we vary ϕ, the height of the first peak of $g(r)$, g_1, varies in a nonmonotonic fashion and has a maximum at $\phi = \phi^*$. There is also a dramatic reduction in the particle mobility near the same value of the packing fraction. This maximum in g_1 is a vestige of the zero-temperature jamming transition. The value of ϕ^* is greater than ϕ_c, the packing fraction where jamming would occur at $T = 0$. These observations are qualitatively consistent with recent simulations [26] and two-dimensional experiments using bidisperse soft colloids [13].

The fact that g_1, the first peak in $g(r)$, is highest at ϕ^* suggests that the sample at ϕ^* may have more medium- and long-range order than at other packing fractions. Indeed, at ϕ^*, we observe that $g(r)$ has at least 14 evenly spaced peaks that decay in height as r increases. This structure does not vary dramatically for $\phi > \phi^*$. This suggests that most of the salient structural features of the system are frozen in when the system first becomes jammed as it passes through ϕ^*. However, the damping of the higher-order peaks increases rapidly as ϕ is decreased below ϕ^*. We see no evidence of a split second peak in $g(r)$ as is seen in simulations [27] and in hard-colloidal systems at the colloidal glass transition [28].

In the next section, we will describe the experimental methods for creating the samples and for measuring the structure and mobility of the systems as a function of packing fraction. In Sec. III, we report our results for the behavior of the pair-correlation function and in particular for how the first peak in $g(r)$ varies with ϕ. We also describe how the dynamics of the particles become dramatically slower near the same packing fraction where g_1 has its maximum value. Finally in Sec. IV, we discuss the implications of our results for understanding the jamming transition at finite temperatures.

II. METHODS AND MATERIALS

We synthesize poly N-isopropyl acrylamide (pNIPAM) colloids using surfactant-free emulsion polymerization [29,30]. The pNIPAM colloids are uniformly dyed with a rhoadamine-based dye so that they can be imaged using fluorescent microscopy. The size, stiffness, and temperature dependence of the colloids is highly sensitive to the details of the synthesis and each batch must be calibrated independently. The colloids are an open cross-linked polymer mesh in water [31]. At packing fractions less than $\phi = 1.0$ the colloids distort while conserving their internal volume [32]. Above $\phi = 1.0$ the particles can de-swell and interpenetrate in addition to distorting [33]. This compression and distortion of colloids is sufficiently small so as not to be visualized by light microscopy and does not negatively impact centroid identification algorithms.

The hydrodynamic particle diameter σ depends on temperature. We measure $\sigma(T)$ by observing the diffusion of the colloids in a dilute sample. The sample temperature, measured to a precision of $0.1°$ C, is controlled with a Bioptechs objective heater thermally coupled to the sample via the objective immersion fluid. As shown in Fig. 1(a), over the range $24°$ C$< T < 34°$ C, the diameter varies by nearly a factor of 2. The data for $\sigma(T)$ is empirically fit by two linear segments connected by a cubic spline. Above $35°$ C, the colloids collapse to a constant size [29]. We assume that the hydrodynamic particle diameter is also the extent of the
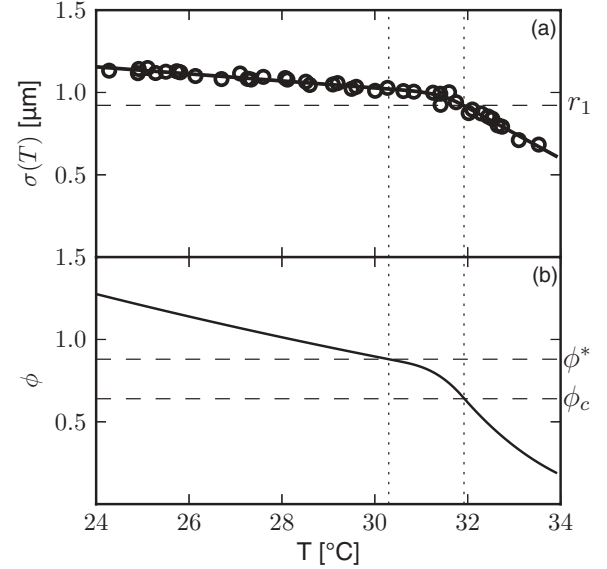

FIG. 1. (a) The hydrodynamic diameter σ versus temperature T of the pNIPAM colloids used in the experiments. The solid line is an empirical fit to the data (open circles). The horizontal dashed line is the average nearest-neighbor spacing r_1 for the number density n used in the experiments. (b) Absolute packing fraction versus T for the n used in the experiments. Vertical dotted lines in both graphs show the temperature where $\phi = \phi^*$ and $\phi = \phi_c$.

particle's finite-range repulsion. The polydispersity is less than 10%, which is the bound we can set by measuring the variation in individual particle diffusion constants. We note, however, that this synthesis protocol typically produces colloids with an even smaller polydispersity of around 3% as measured by dynamic light scattering [13].

We estimate the packing fraction of dense systems from the particle diameter σ and the number density n

$$\phi(T) = \frac{\pi}{6} n \sigma(T)^3. \tag{1}$$

To determine the absolute packing fraction for our system, we first determine the number density of our system. At ϕ_c and $T = 0$, $r_1 = \sigma$. We substitute this into Eq. (1) to find $n = \frac{6\phi_c}{\pi r_1^3}$ and

$$\phi(T) = \phi_c \left(\frac{\sigma(T)}{r_1} \right)^3. \tag{2}$$

We use $\phi_c = 0.64$, which is the density of random close packing as measured in hard- and soft-sphere simulations and hard-sphere experiments [10,34].

The primary effect of changing the environmental temperature is to change the size of the colloids (and hence ϕ) rather than the thermal energy. Over a $10°$ C temperature range, ϕ varies by a factor of 7 as shown in Fig. 1(b). We take data in the range between $T = 27°$ to $32°$ C, which corresponds to $0.55 < \phi < 1.17$. Over this range, the sample transforms from a liquid state, where the particles are diffusive, to a fully arrested packing.

Sample chambers are made from microscope slides and cover slips and sealed with epoxy (Norland 61). The chambers are small, 0.15 mm $\times 5$ mm $\times 3$ mm, to minimize internal thermal gradients. To prepare dense samples, sparse suspensions

of colloids are centrifuged to sediment the colloids. The suspension is then heated to 35° C to shrink the particles. The sediment is then pipetted into the sample chamber, which is quickly sealed with epoxy so that the total volume and number of particles (and thus the number density n) are fixed. After enclosure in the chamber, the samples are prepared for observation by first heating to 35° C to turn the system into a fluid. Because there is always a danger of crystallization when the particle mobility is large, we quickly quench the system into an amorphous solid by placing the sample chamber onto a 4° C metal surface. This cools the sample in less than 5 s and prevents the nucleation of crystals. This quench protocol consistently generates arrested amorphous configurations. To perform a measurement, we then heat the amorphous solid to obtain the desired ϕ.

Particle dynamics and $g(r)$ were extracted from data sets taken at different discrete values of ϕ. Between subsequent measurements, the sample was melted and requenched. The waiting time from the quench to observation was approximately 900 seconds and was controlled to minimize possible complications due to aging [25,35]. To obtain $g(r)$ in finer increments of ϕ, the packing fraction was also swept continuously. For increasing ϕ ramps, a fluidized sample is placed on a preheated objective. The objective heater was then turned off and the sample was periodically imaged as it cooled slowly to ambient temperature.

We are unable to acquire three-dimensional (3D) stacks rapidly enough to track particle motion accurately at all ϕ of interest. Thus, we acquire two-dimensional (2D) data using the same imaging conditions at all ϕ to avoid possible systematic effects due to varying the imaging conditions. We image a 2D slab far from the boundaries of a 3D sample using a Yokogawa CSU-XI confocal head and a Nikon 60x(N.A. = 1.2) water immersion objective. The images are acquired at frame rates between 0.3 and 10 Hz using a 14 bit-depth Roper Coolsnaps HQ camera. The field of view is $150 \times 111\,\mu$m and contains approximately 20 000 particles. The accuracy of feature identification in the x-y plane is approximately 0.1 pixel in the camera, corresponding to 15 nm in our imaging setup.

Due to the confocal slice having a finite thickness w, particles both above and below the focal plane are imaged as being in the plane. This introduces an uncertainty $w/2 \approx$ 400 nm in the z position of the particle. As a result the measured distance between two particles, which is the distance projected onto the x-y plane, will be less than the true distance. The difference between the measured and true distance is significant at small r but is small when $r \gg w$. This introduces a systematic error in $g(r)$ which can be corrected [36]

$$g(r) \approx g_{\text{raw}}\left[r\left(1 - \frac{1}{12}\frac{w^2}{r^2} + \frac{1}{720}\frac{w^4}{r^4}\right)\right]$$
$$+ \frac{7}{1440}\frac{w^4}{r^4}r^2\left.\frac{d^2 g_{\text{raw}}}{dr^2}\right|_r, \qquad (3)$$

where g_{raw} is the pair-correlation function measured prior to taking into account the effects of projection. We have used simulations to check the validity of this approximation.

The correction shifts peaks towards larger r, increases peak heights, and decreases the valleys of $g(r)$. It primarily affects
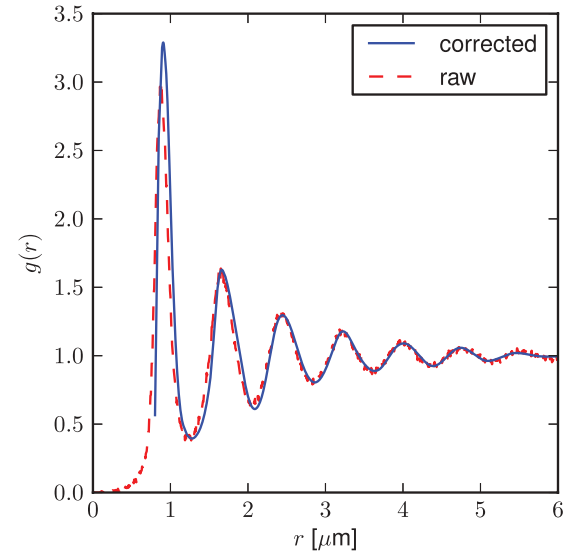

FIG. 2. (Color online) The corrected (solid) and raw (dashed) $g(r)$ curves for a sample at $\phi = \phi^*$. The correction accounts for the finite thickness of the slab imaged by the confocal microscope. The correction becomes progressively smaller at larger r and is only significant for the first peak of $g(r)$.

the first peak of $g(r)$. This is shown in Fig. 2. The position of the first peak is shifted by 4% and its height is enhanced by 10%. The effect on higher-order peaks is significantly smaller. The projection is present in all of our data sets and will not effect the relative measurements as a function of ϕ. At large r the primary source of the noise in $g(r)$ is from undersampling configuration space.

The data are processed using a locally developed C++ implementation of the Crocker-Grier feature identification and tracking algorithm [37] incorporating an existing implementation of the identification routine [38]. Particles are identified using a two-pass feature identification algorithm. The first pass identifies to pixel resolution the local intensity maximum corresponding to particle centers. The second pass computes the center of mass in a window around the local maximum to achieve subpixel resolution. The tracking algorithm links particles in sequential frames by minimizing the total magnitude of frame-to-frame displacement. Our tracking and correlations software is available at [39] and is an order of magnitude faster than equivalent code written in an interpreted language.

III. RESULTS AND DISCUSSION

We will first discuss some of the general features of the pair-correlation function. In Sec. III A, we describe the dependence of $g(r)$ on the packing fraction and in Sec. III B, we discuss the long-range correlations seen in $g(r)$. In Sec. III C, we describe our measurements of the particle mobility.

Figure 3 shows the pair-correlation function at different ϕ. These data have been corrected for the projection issues discussed in Sec. II. In each case, there is a large first peak at $r_1 \approx 0.9\,\mu$m. At the lowest ϕ shown, only the first three peaks are large enough to be easily discerned. As ϕ is increased, the peaks at larger r grow and become clearly visible.
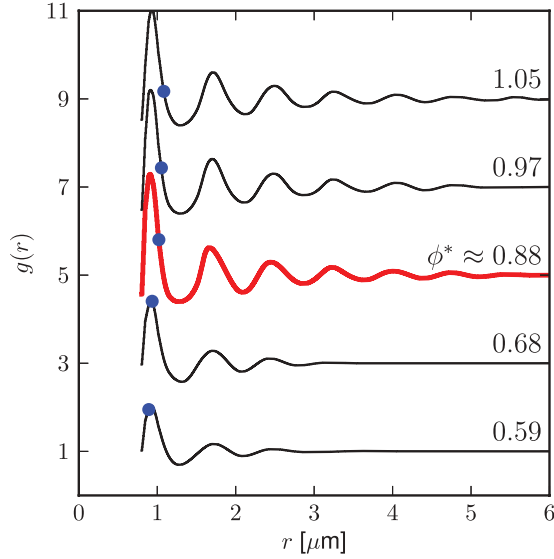
FIG. 3. (Color online) The pair-correlation function $g(r)$ at different packing fractions ϕ. For clarity the curves are shifted vertically by 2 for each successive packing fraction. The data have been corrected for the projection effects discussed in the text. All but the bottom curve have $\phi > \phi_c$. The thick (red) curve is for $\phi \approx \phi^*$. The position of the first peak remains fixed even though the nominal particle diameter varies as indicated by the dot on each curve.

The position of the first peak, r_1, does not shift appreciably even though the packing fraction varies by a factor of 1.7. To emphasize this point, the nominal particle diameter σ is marked on each curve in Fig. 3. At all $\phi > \phi_c$, $\sigma > r_1$, indicating that the particles strongly interact with and deform their neighbors. Despite this, we can easily detect the particles and measure their positions as shown in Fig. 4. This insensitivity of the peak position occurs because the average interparticle spacing in this densely packed system is set by the number density n, which is held constant.
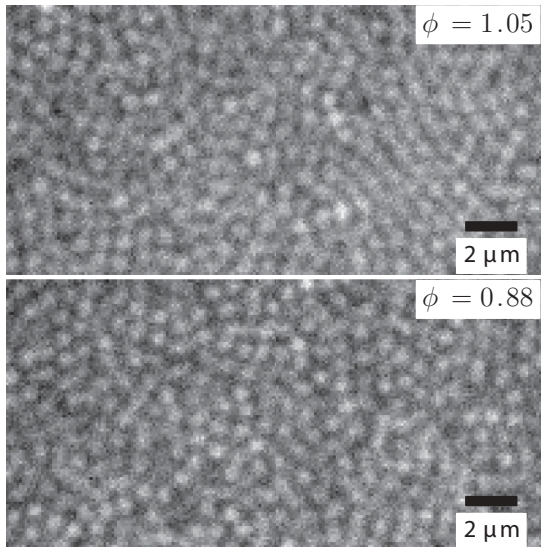

FIG. 4. Raw 22×11-μm section from the images used to generate the $\phi = 1.05$ and $\phi = 0.88$ curves in Fig. 3.

A. Behavior of first peak of $g(r)$: Vestige of the jamming transition

In Fig. 5, we plot the height of the mth peak g_m of the first three peaks in $g(r)$ versus ϕ. We measure g_m in two protocols: (i) We quench the sample rapidly to a desired ϕ and (ii) we slowly and continuously ramp the packing fraction. The two protocols yield nearly identical results showing that the data are not significantly affected by aging or by transient effects.

The first peak, g_1, has nonmonotonic behavior. Starting at small ϕ, g_1 grows with ϕ until it reaches a maximum value at $\phi \equiv \phi^* = 0.88 \pm 0.02$ and then decreases as ϕ is increased further. Within the error bars of our measurement, the peaks $m = 2,3$ grow monotonically until they reach a plateau value at ϕ^*.

The behavior in g_1 is consistent with the experiments [13] and simulations [26] on thermal 2D bidisperse systems. As in those cases, we interpret the peak in g_1 as a vestige of the $T = 0$ jamming transition; it is due to the interplay between particle overlap caused by thermal motion and particle overlap due to geometric constraints, as described in [13]. This leads to a peak in g_1 versus ϕ as observed. ϕ^*, where g_1 is a maximum, is
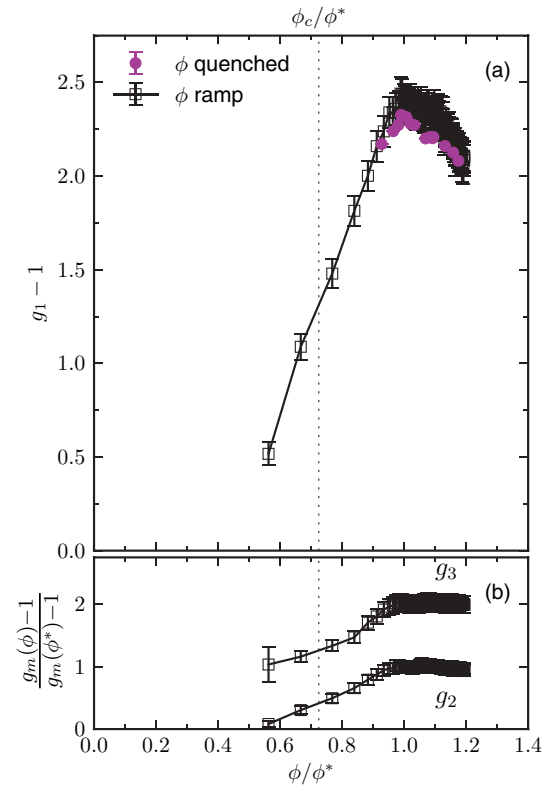

FIG. 5. (Color online) (a) Height of the first peak of the pair-correlation function versus packing fraction. $g_1 - 1$ is plotted versus normalized packing fraction ϕ/ϕ^* for both quenched and ramped experiments. The maximum in the height of the first peak is clearly present in both measurement protocols. (b) The values of $g(r)$ for the quenched data evaluated at the second and third peaks. $g_2 - 1$ and $g_3 - 1$ normalized by their values at ϕ^* are plotted versus ϕ/ϕ^*. For clarity the curve for the third peak is shifted vertically by 1. Both peaks increase with ϕ up to ϕ^* and then plateau above ϕ^*. Neither peak shows a maximum versus packing fraction outside of our noise level. In both plots the vertical dotted line indicates ϕ_c/ϕ^*.

necessarily shifted to $\phi > \phi_c$ by the thermal motion. Its value will therefore depend on the thermal energy in the system. In our 3D samples, ϕ^* is shifted above ϕ_c by a much greater amount than was reported in 2D [13].

B. Structure: Long-range correlations

The pNIPAM particles are soft yet they show a tall, well-defined first peak in $g(r)$ qualitatively similar to hard-sphere systems [3]. However, for soft spheres the rise at low r in the first peak in $g(r)$ is steep but is not a step function since the particles can deform or overlap. There is an even more dramatic difference: in hard-sphere experiments [3] and simulations at $T = 0$ [10,27], a split second peak is observed. This splitting has been used as a possible signature to identify colloidal glasses [28]. However, our soft-sphere amorphous packings, as demonstrated by Figs. 3 and 6, show no sign of a split second peak at any ϕ.

At large ϕ, many peaks, corresponding to higher-order coordination shells, are visible. The height of these peaks decays at large r. Remarkably, as shown in Fig. 6, near ϕ^*, we can identify at least 14 peaks in $g(r)$. The smallest of these is a fluctuation of less than 1% from uniform density as seen in the inset. We are unaware of any other experiment that identifies as many peaks in an amorphous sample.

Figures 6(b) and 6(c), respectively, plot the peak height $g_m - 1$ and location r_m versus peak number m. We can fit the

decay envelope to the Percus-Yevic asymptotic form

$$g_m - 1 = C \frac{\exp\left(\frac{r_m}{\xi}\right)}{r_m}, \qquad (4)$$

where r_m is the location of the mth peak and C and ξ are fitting parameters that depend on ϕ [40]. At ϕ^* $C = 2.31$ and $\xi = (-2.6 \pm 0.1)r_1$, which is a longer correlation length than seen in the hard-sphere simulations and experiments [41,42].

Beyond the first peak, the interpeak spacing is very uniform: the location of the mth peak, r_m, is accurately given by

$$r_m/r_1 = 1 + (0.85 \pm 0.02)(m - 1), \qquad (5)$$

as shown in Fig. 6(c). This spacing holds at all ϕ where we see enough peaks to fit a line to the spacing. The peak spacing is in quantitative agreement with what has been observed in other systems: hard-sphere colloids [42], ball bearings [34], simulations at ϕ_c [41], and experimental measurements of liquid noble gases [34], despite the drastically different interparticle potentials and temperatures. This suggests a fundamental geometric origin for this peak spacing.

These two results taken together imply that beyond the first peak, $g(r)$ can be approximated by a damped sinusoid

$$g(r) = 1 + \frac{C}{r} \exp\left(\frac{r}{\xi}\right) \cos\left(2\pi \frac{r - r_1}{0.85 r_1}\right). \qquad (6)$$

This form is shown as the thin dotted line in Fig. 6(a). This form is roughly consistent with a wide range of analytic [43], simulation [41,44], and experimental [42] results and indicative of a dense fluid structure.

C. Dynamics: Slowing at ϕ^*

We now investigate whether the packing fraction ϕ^*, where g_1 has a peak, is associated with any change in the particle dynamics in the sample. To quantify the particle mobility we use the van Hove correlation function

$$P(\Delta_x, \tau) = \frac{1}{N_0} \left\langle \sum_i \delta[x_i(t) - x_i(t + \tau) - \Delta_x] \right\rangle, \qquad (7)$$

where $x_i(t)$ is the x component of the ith particle location at time t, $\langle \rangle$ is an average over all starting times, and N_0 is a normalization constant such that $\int d\Delta_x \, P(\Delta_x, \tau) = 1$. $P(\Delta_y, \tau)$ is similarly defined. Physically $P(\Delta_x, \tau)$ is the probability of a particle moving a distance Δ_x in the x direction in a time τ. The mobility is isotropic in all directions, as demonstrated by Figs 7(a) and 7(c). Data for both $P(\Delta_x, \tau)$ and $P(\Delta_y, \tau)$ are shown and are indistinguishable. We also measure the distribution of the displacements of a given magnitude $P(|\vec{\Delta}|, \tau)$, which uses the data for the displacements in all directions.

There is a qualitative change in particle mobility as the packing fraction approaches ϕ^*. This change is evident in the shape of $P(\Delta_x, \tau = 1.6 \, \text{s})$ shown in Fig. 7(a). the curves for $\phi < \phi^*$ and $\phi > \phi^*$ are plotted as dashed and solid lines, respectively.
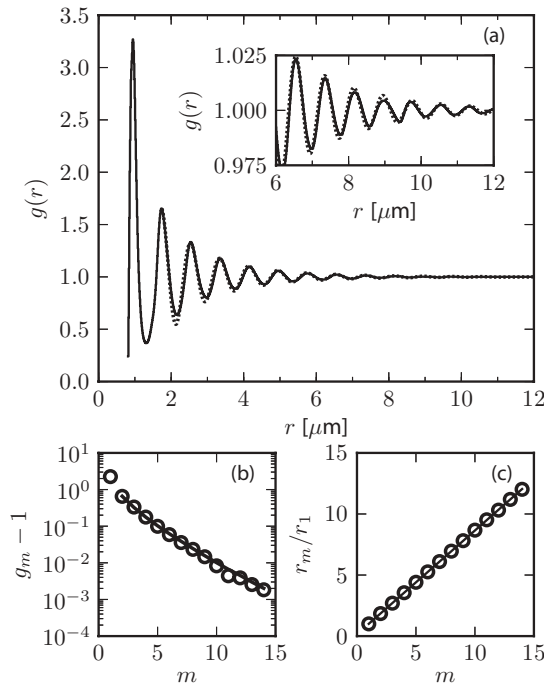

FIG. 6. (a) The pair-correlation function $g(r)$ for $\phi = 0.99\phi^*$. The dotted line is the fit of Eq. (6). The inset shows a magnification of the data for the peaks beyond $r = 6 \, \mu\text{m}$. (b) Peak height $g_m - 1$ versus peak number m. $g_m - 1$ is fit to the decay form of Eq. (4). (c) Peak location r_m/r_1 versus m. The peak locations are evenly spaced and can be fit to a straight line, Eq. (5), with slope 0.85.
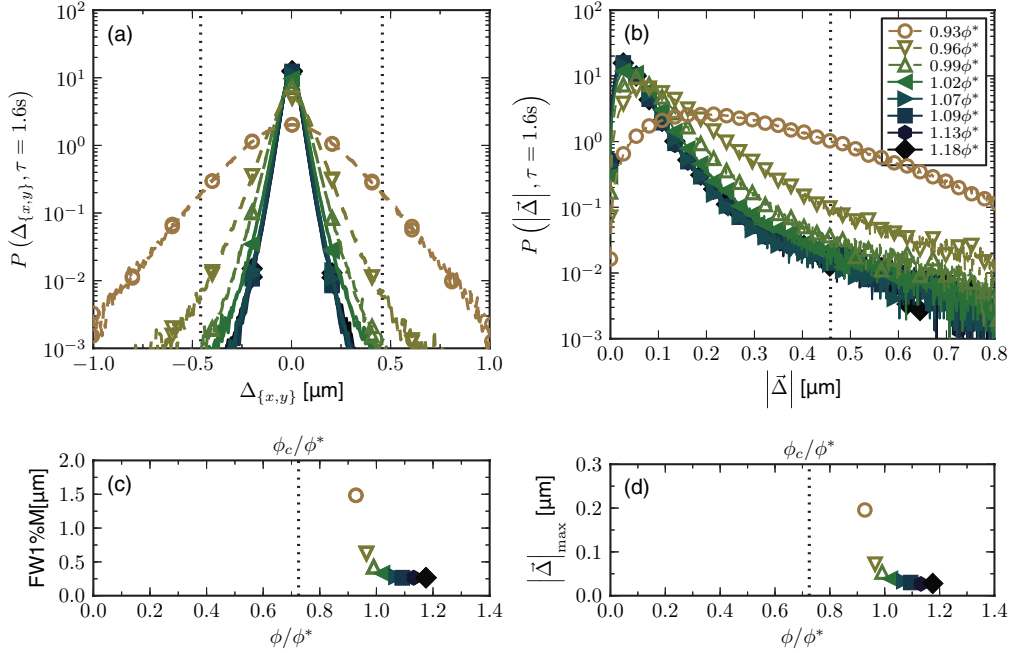
FIG. 7. (Color online) (a) van Hove correlation functions for $\tau = 1.6$ s. (a) $P(\Delta_x)$ and $P(\Delta_y)$ showing the symmetry around $\Delta = 0$ for a range of ϕ. The motions along the two axes are statistically indistinguishable. (b) $P(|\Delta|)$ versus the absolute value of the displacement Δ. In (a) and (b) systems where $\phi < \phi^*$ are shown with dashed lines and open symbols, those where $\phi > \phi^*$ are shown with solid lines and closed symbols. The vertical dotted lines indicate half the average particle spacing. In (a) the curves for $\phi > 1.07\phi^*$ cannot be distinguished because they lie under the curve at $1.07\phi^*$. (c) The full width at 1% max versus ϕ. The width decreases rapidly with packing fraction up to $\phi/\phi^* \approx 1$ and is approximately constant above it. The widths of $P(\Delta_x)$ and $P(\Delta_y)$ are identical to the resolution of our data. (d) The location of the peak of $P(|\Delta|)$ versus ϕ/ϕ_*. In (c) and (d), the vertical dotted lines indicate ϕ_c/ϕ^*.

At the lowest ϕ plotted, $0.93\phi^*$, the distribution is nearly Gaussian and a significant number of particles move more than $r_1/2$ (shown by the dotted vertical lines), indicating a substantial rearrangement of the packing on the 1.6 s time scale. As ϕ is increased, $P(\Delta_x)$ and $P(\Delta_y)$ narrow. Above $1.07\phi^*$, the curves are nearly indistinguishable and lie on top of each other. In this dense state, the particles are essentially arrested on the time scales probed. Even at these large values of ϕ, the error in finding particle positions is much smaller than the width of the distributions measured.

To look at a measure of mobility which does not select any special direction in space, we plot $P(|\vec{\Delta}|, \tau = 1.6$ s$)$ in Fig. 7(b). This shows the same trend as $P(\Delta_x)$ and $P(\Delta_y)$. The peak in $P(|\vec{\Delta}|, \tau = 1.6$ s$)$ moves to smaller $|\vec{\Delta}|$ as ϕ increases. Above $\phi = 1.07\phi^*$, the position no longer evolves. Figures 7(c) and 7(d) show, respectively, how the curves for $P(\Delta_{\{x,y\}}, \tau = 1.6$ s$)$ narrow and the peak position of $P(|\vec{\Delta}|, \tau = 1.6$ s$)$ decreases as ϕ is increased.

We can compute the 3D mean-squared displacement of the particles $\overline{\Delta^2}(\tau)$ in time τ plotted in Fig. 8(a). For comparison, the expected $\overline{\Delta^2}(\tau)$ for a dilute sample is shown as the dotted line. At the lowest ϕ the particles are nearly diffusive, but with a diffusion constant significantly reduced from the dilute limit. The narrowing of $P(\Delta_x, \tau)$ is reflected in the vertical shift of the curves and is accompanied by a suppression of the slope. If we assume that $\overline{\Delta^2}(\tau) \propto \tau^\alpha$, then the by fitting the slope we can extract $\alpha(\phi)$, shown in Fig. 8(b). Although from our data, which have a limited range in τ, we are unable to observe

either very early or very late times, there is nonetheless a clear change in dynamics in the neighborhood of ϕ^*. This change does not have a sharp signature but occurs over a range in ϕ.

It is tempting to associate the dynamical arrest at ϕ^* with the vestige of the jamming transition. However, this is problematic because the peak in g_1 is an unambiguous geometric signature and does not display aging effects, whereas the dynamical signature is not sharp and depends on the experimental time scale used to perform the measurements.

It has been argued that the particle mobility can be derived from the pair-correlation function [45]. However, in Fig. 9 we compare $g(r)$ at $0.96\phi^*$ and $1.07\phi^*$, with $\alpha = 0.32$ and $\alpha = 0.10$, respectively, and we see that despite the difference in particle mobility, the structure is experimentally indistinguishable. In the inset of Fig. 9, we show the difference between the raw data: $\Delta q \equiv g_{\text{raw}}(r; \phi = 0.96\phi^*) - g_{\text{raw}}(r; \phi = 1.07\phi^*)$. (We use raw data to avoid comparing possible artifacts introduced by the correction.) The average of $|\Delta q|$ is 0.006. These results are potentially problematic for mode-coupling theory as we have experimentally shown that the same static structure can give rise to very different dynamics [46]. This disconnect between the structure and dynamics is in agreement with recent work that showed that, by using different potentials, configurations with very similar $g(r)$ can have very different dynamics [47]. It would be important to be able to compare with a theoretical estimate of how much the pair-correlation function would have to change to produce the observed variation in the dynamics. To our knowledge such an estimate is not available.
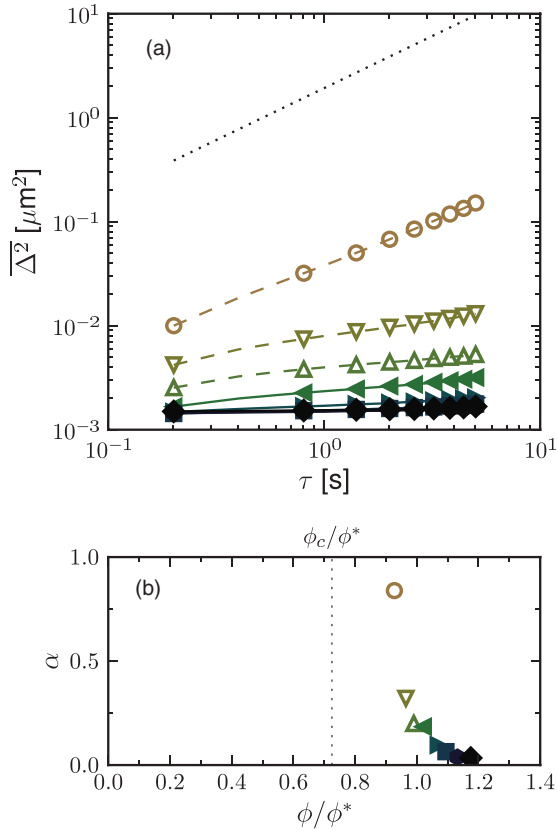
FIG. 8. (Color online) (a) Mean-squared particle displacement versus τ for different values of ϕ. The symbols and colors match those in Fig. 7. The dotted line indicates the expected diffusion in a dilute sample. (b) The slope of the lines in (a) α versus ϕ/ϕ^*. At $\phi < \phi^*$ the system is nearly diffusive despite the particles strongly interacting with their neighbors. The vertical dashed line indicates ϕ_c/ϕ_*.

IV. CONCLUSION

We have demonstrated that there is a peak in g_1 as a function of ϕ in a 3D packing of soft pNIPAM colloids undergoing Brownian motion. This is a vestige of the $T = 0$ jamming transition that survives at finite temperature and is consistent with previous experiments in 2D systems [13]. It has been argued that such a peak in g_1 can be derived from an analysis of the liquid state without reference to jamming explicitly [48]. This does not mean that it is not a vestige of the zero-temperature jamming transition. The $T = 0$ jamming transition is the point at which the competition between thermal effects and compression is the most pronounced. At that point, *everything* is governed by compression because the temperature is zero. This is what leads to the δ function at $r = \sigma$. Temperature acts to smear out this sharp structure as the motion of the particles can create overlap even if the packing fraction is lower than ϕ_c. The physics of the effect at high temperatures is in fact described [48] by the same general considerations that had been earlier [13] used to understand this behavior near the $T = 0$ jamming transition.

In contrast with the results in two dimensions [13], the packing fraction, ϕ^*, where g_1 has a peak is significantly higher
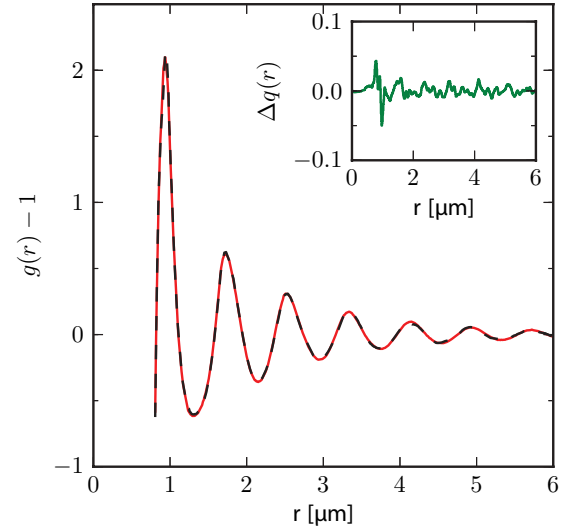

FIG. 9. (Color online) The corrected pair-correlation function $g(r)$ at $0.96\phi^*$ and $1.76\phi^*$. Inset: The difference between the raw pair-correlation data $\Delta q \equiv g_{\mathrm{raw}}(r; \phi = 0.96\phi^*) - g_{\mathrm{raw}}(r; \phi = 1.07\phi^*)$ is zero within the experimental resolution despite the difference in particle mobility.

than ϕ_c, the packing fraction where particles would first jam at $T = 0$. This indicates that, although the system is very far from the jamming point, aspects of the jamming transition are still observed in the sample's structure. We have also shown that the dynamics of our soft colloid fluid will become very slow (that is, arrested on the time scale of our experiments) when the packing fraction is increased above ϕ^*. This is an example of a pressure-induced glass transition [7,49–52].

We have also observed that the pair-correlation function for this soft-sphere system has features expected of a fluid. For example, the second peak in $g(r)$ is smooth with no sign of any splitting that is characteristic of hard-sphere systems. Moreover, near ϕ^*, we observe up to 14 equally spaced peaks in $g(r)$ whose amplitudes decay as a function of distance in a fashion that is also consistent with the predictions of liquid structure. As the packing fraction is decreased below ϕ^*, the damping of the peaks becomes much more dramatic so that near ϕ_c only three peaks are clearly visible. We observe that in Fig. 5, g_1 increases rapidly at low ϕ until it reaches a peak, but then decreases more gradually above ϕ^*. This asymmetry around the peak can be related to how the contributions to the overlap of particles from thermal motion and from pressure vary with the packing fraction. The role of temperature in broadening the first peak rapidly becomes less important as the packing fraction is increased [13].

Because the pNIPAM colloids are so soft, it is possible to have a very large particle overlap. This not only changes the structure of $g(r)$, but also allows the system to be diffusive at packing fractions ϕ that are inaccessible to hard spheres. Further studies are needed on the dynamics in the neighborhood of ϕ^*, particularly in comparison to the dynamical heterogeneity and correlated motion observed in hard-sphere packings near ϕ_c [15]. This system may also be used to measure the density of states to determine if the dynamical predictions [8] at $T = 0$ extend to $T > 0$ in three dimensions.

[1] P. Chaikin and T. C. Lubensky, *Principles of Condensed Matter Physics* (Cambridge University Press, Cambridge, England, 2000).

[2] L. E. Busse and S. R. Nagel, Phys. Rev. Lett. **47**, 1848 (1981).

[3] A. van Blaaderen and P. Wiltzius, Science **270**, 1177 (1995).

[4] H. R. Wendt and F. F. Abraham, Phys. Rev. Lett. **41**, 1244 (1978).

[5] S. Basak, R. Clarke, and S. R. Nagel, Phys. Rev. B **20**, 3388 (1979).

[6] E. Corwin, H. Jaeger, and S. Nagel, Nature (London) **435**, 1075 (2005).

[7] A. Liu and S. Nagel, Nature (London) **396**, 21 (1998).

[8] A. J. Liu and S. R. Nagel, Annu. Rev. Condens. Matter Phys. **1**, 347 (2010).

[9] M. van Hecke, J. Phys.: Condens. Matter **22**, 033101 (2010).

[10] C. S. O'Hern, L. E. Silbert, A. J. Liu, and S. R. Nagel, Phys. Rev. E **68**, 011306 (2003).

[11] P. Chaudhuri, L. Berthier, and S. Sastry, Phys. Rev. Lett. **104**, 165701 (2010).

[12] M. Otsuki and H. Hayakawa, Phys. Rev. E **86**, 031505 (2012).

[13] Z. Zhang, N. Xu, D. T. N. Chen, P. Yunker, A. M. Alsayed, K. B. Aptowicz, P. Habdas, A. J. Liu, S. R. Nagel, and A. G. Yodh, Nature (London) **459**, 230 (2009).

[14] F. Sciortino and P. Tartaglia, Adv. Phys. **54**, 471 (2005).

[15] E. R. Weeks, J. C. Crocker, and D. A. Weitz, J. Phys.: Condens. Matter **19**, 205131 (2007).

[16] P. Schall, D. A. Weitz, and F. Spaepen, Science **318**, 1895 (2007).

[17] J. C. Conrad, P. P. Dhillon, E. R. Weeks, D. R. Reichman, and D. A. Weitz, Phys. Rev. Lett. **97**, 265701 (2006).

[18] E. Weeks and D. Weitz, Chem. Phys. **284**, 361 (2002).

[19] E. R. Weeks and D. A. Weitz, Phys. Rev. Lett. **89**, 095704 (2002).

[20] E. R. Weeks, J. C. Crocker, A. C. Levitt, A. Schofield, and D. A. Weitz, Science **287**, 627 (2000).

[21] W. K. Kegel and A. van Blaaderen, Science **287**, 290 (2000).

[22] J. M. Lynch, G. C. Cianci, and E. R. Weeks, Phys. Rev. E **78**, 031410 (2008).

[23] U. Gasser, A. Schofield, and D. A. Weitz, J. Phys.: Condens. Matter **15**, S375 (2003).

[24] G. Cianci, R. Courtland, and E. Weeks, Solid State Communications **139**, 599 (2006).

[25] R. E. Courtland and E. R. Weeks, J. Phys.: Condens. Matter **15**, S359 (2003).

[26] L. Wang and N. Xu, Soft Matter, doi: 10.1039/C2SM27148F.

[27] L. E. Silbert, A. J. Liu, and S. R. Nagel, Phys. Rev. E **73**, 041304 (2006).

[28] M. Jenkins and S. Egelhaaf, Adv. Colloid Interface Sci. **136**, 65 (2008).

[29] R. Pelton, Adv. Colloid Interface Sci. **85**, 1 (2000).

[30] B. Saunders and B. Vincent, Adv. Colloid Interface Sci. **80**, 1 (1999).

[31] I. Varga, T. Gilányi, R. Mészáros, G. Filipcsei, and M. Zrínyi, J. Phys. Chem. B **105**, 9071 (2001).

[32] K. N. Nordstrom, E. Verneuil, W. G. Ellenbroek, T. C. Lubensky, J. P. Gollub, and D. J. Durian, Phys. Rev. E **82**, 041403 (2010).

[33] U. Gasser, J.-J. Lietor-Santos, J. S. Hyatt, E. S. Herman, P. Mohanty, J. Crassous, K. van Gruijthuijsen, D. Paloli, M. Obiols-Rabasa, A. Stradner, P. Schurtenberger, L. A. Lyon, and A Fernandez-Nieves (unpublished).

[34] G. D. Scott, Nature (London) **194**, 956 (1962), and references therein.

[35] S. Mazoyer, L. Cipelletti, and L. Ramos, Phys. Rev. E **79**, 011501 (2009).

[36] H. Totsuji, J. Phys. Soc. Jpn. **78**, 065004 (2009).

[37] J. C. Crocker and D. G. Grier, J. Colloid Interface Sci. **179**, 298 (1995).

[38] P. J. Lu, P. A. Sims, H. Oki, J. B. Macarthur, and D. A. Weitz, Opt. Express **15**, 8702 (2007).

[39] https://github.com/tacaswell/tracking.

[40] P. Perry and G. J. Throop, J. Chem. Phys. **57**, 1827 (1972).

[41] A. Donev, F. H. Stillinger, and S. Torquato, Phys. Rev. Lett. **95**, 090604 (2005).

[42] R. Kurita and E. R. Weeks, Phys. Rev. E **82**, 011403 (2010).

[43] E. Matteoli and G. A. Mansoori, J. Chem. Phys. **103**, 4672 (1995).

[44] D. M. Heyes, S. M. Clarke, and A. C. Brańka, J. Chem. Phys. **131**, 204506 (2009).

[45] D. R. Reichman and P. Charbonneau, J. Stat. Mech.: Theory Exp. (2005) P05013.

[46] L. Berthier and G. Tarjus, Phys. Rev. E **82**, 031502 (2010).

[47] L. Berthier and G. Tarjus, J. Chem. Phys. **134**, 214503 (2011).

[48] H. Jacquin and L. Berthier, Soft Matter **6**, 2970 (2010).

[49] K. Z. Win and N. Menon, Phys. Rev. E **73**, 040501 (2006).

[50] T. Atake and C. A. Angell, J. Phys. Chem. **83**, 3218 (1979).

[51] A. Reiser, G. Kasper, and S. Hunklinger, Phys. Rev. B **72**, 094204 (2005).

[52] S. L. Shumway, A. S. Clarke, and H. Jónsson, J. Chem. Phys. **102**, 1796 (1995).